

Optimum Model-Based Segmentation Techniques for Multifrequency Polarimetric SAR Images of Urban Areas

Pierfrancesco Lombardo, *Member, IEEE*, Massimo Sciotti, Tiziana Macrí Pellizzeri, and Marco Meloni

Abstract—A new technique, named diagonal polarimetric merge-using-moments (DPOL MUM), is proposed for the segmentation of multifrequency polarimetric synthetic aperture radar (SAR) images that exploits the characteristic block diagonal structure of their covariance matrix. This technique is based on the newly introduced split–merge test, which has a reduced fluctuation error than the straight extension of the polarimetric test (POL MUM) and is shown to yield a more accurate segmentation on simulated SAR images. DPOL MUM is especially useful in the extraction of information from urban areas that are characterized by the presence of different spectral and polarimetric characteristics. Its effectiveness is demonstrated by applying it to segment a set of SIR-C images of the town of Pavia. The classification of the image segmented with DPOL MUM shows higher probability of correct classification compared to POL MUM and to a similar technique that does not use the correlation properties (MT MUM).

Index Terms—Polarimetry, multifrequency, unsupervised segmentation, urban areas.

I. INTRODUCTION

IT IS WELL KNOWN that multifrequency polarimetric synthetic aperture radar (SAR) images carry appreciably more information about the observed scene than the single-channel SAR images. In particular, the specific reflectivity at the different frequencies and both the reflectivity and the phase relationship between the different polarimetric channels provide useful indications on the characteristics of the different observed objects, allowing a more accurate classification [1]–[4]. This is especially important in the complex urban environment, where a small area contains a very high variety of different behaviors both in frequency and polarization, and a high sensitivity to these differences would be largely useful to extract more information from the remotely sensed data. Many examples of both segmentation and terrain classification using polarimetric SAR data can be easily found in literature, with application to very different monitoring and surveillance applications [5]–[10]. Many proposed techniques to operate with polarimetric SAR images are suited to pixel-by-pixel classification on the basis of the polarimetric properties, whereas it has been clearly demonstrated (see [1] and [11]) that large performance improvement can be achieved by first segmenting the image into regions with homogeneous characteristics, and then classifying the resulting global regions. It is

therefore of interest to define optimal segmentation techniques for the multifrequency polarimetric SAR images. Moreover, it has been shown that the use of multifrequency polarimetric SAR images yields a further improvement in the possibility to identify and classify homogeneous regions with slightly different terrain characteristics.

An effective approach for the segmentation of polarimetric SAR images has been proposed in [12] and [13], which can easily be extended to perform the joint segmentation of any set of complex correlated SAR images and therefore also to the case of multifrequency polarimetric images. However, the corresponding large increase of dimensionality implies also an increased level of uncertainty in the underlying test, which is a potential source of performance degradation. However, it is usual to model the images acquired at different frequencies as uncorrelated. This is also the case for many other situations, as the case of multitemporal sets of images collected with low revisit time. The exploitation of this model, which corresponds to a block diagonal covariance matrix for the multifrequency polarimetric images, can largely reduce the uncertainty in the segmentation test and yield much better performance than the simple extension of the polarimetric segmentation scheme. Therefore, the aim of this paper is to derive optimal segmentation techniques that fully exploit the statistical model of the multifrequency polarimetric SAR images, and to evaluate their performance both theoretically and on simulated data. The application to a set of SAR images of urban areas shows the practical results obtained with the proposed technique.

The proposed techniques use a generalized maximum-likelihood (ML) approach, based on the joint probability density function (pdf) of the pixels in each homogeneous region. In particular, we adopt a multivariate Gaussian model to describe the statistical behavior of the single channels (and therefore a complex Wishart model for the distribution of the corresponding multilook complex data); thus, the statistical characteristics of the different regions are encoded in the covariance matrix. The proposed segmentation techniques are based on the use of an optimal split–merge test to merge regions with similar characteristics (region fusion), and they are totally unsupervised. The generalized likelihood ratio test is used to derive the optimal test to decide whether two adjacent regions should be split or merged. The likelihood function is also the basis of the proposed supervised classification technique. Section 2 reports the derivation of the ML segmentation technique presented in [12] and [13], which makes no assumption on the structure of the covariance matrix and is particularly suited for monofrequency,

Manuscript received September 16, 2002; revised March 21, 2003. This work was supported in part by the Italian Space Agency (ASI).

The authors are with INFOCOM Department, University of Rome “La Sapienza,” 00184 Rome, Italy (e-mail: t.macri.pellizzeri@infocom.uniroma1.it).
Digital Object Identifier 10.1109/TGRS.2003.814632

monotemporal polarimetric images. As mentioned above, this technique can be immediately extended to process multiparametric datasets. In Section 3, we consider the case of a covariance matrix with a special known structure that can be used as *a priori* information to reduce the losses introduced by its local estimation performed inside the algorithm. In particular, we consider the case of a block diagonal structure for the covariance matrix, which is usually the case for multifrequency or multi-temporal polarimetric SAR data. Thus, we derive a ML segmentation technique specifically designed for this case. In Section 4 a theoretical performance analysis of the optimum model-based split-merge test is presented. The analysis is used to set the appropriate thresholds for the test as a function of the desired false-alarm probability and the regions size. Simulation is then adopted to confirm these predictions. Moreover, the two proposed approaches are compared, showing that the use of the *a priori* information about the covariance matrix structure results in an increased capability to discriminate regions with different characteristics. Section 5 presents the results of a thorough analysis of the segmentation performance of the proposed technique. To this purpose, a test pattern is defined to generate simulated SAR images with different characteristics. Also a comparison of the results obtained by classifying the segmentation outputs is reported. In Section 6 the proposed segmentation techniques are applied to a set of polarimetric and multifrequency (C and L band) SIR-C images of the town of Pavia, in northern Italy. Finally, our conclusions are drawn in Section 7, while the mathematical details are reported in Appendix A and B.

II. ML POLARIMETRIC SEGMENTATION

Let us assume that we operate on fully calibrated polarimetric SAR images, in order to focus on the polarimetric signal processing techniques only (for details on calibration procedures and problems see [14]). Consider a single region and arrange the echoes received from the same resolution cell on the M polarimetric channels into the M -dimensional vector, $\mathbf{x} = [x_1, \dots, x_M]^T$, (where for example $x_1 = x_{HH}, x_2 = x_{VV}, x_3 = x_{HV}$). Assuming the absence of texture in the SAR image, the joint pdf of the N pixels of a single region can be written as

$$p(\mathbf{x}) = \frac{1}{\pi^{MN} |\mathbf{R}|^N} \exp \left[-\text{Tr} \left\{ \mathbf{R}^{-1} \sum_{n=1}^N \mathbf{x}_n \mathbf{x}_n^H \right\} \right] \quad (1)$$

where \mathbf{R} is the polarimetric complex covariance matrix and $\text{Tr}\{\mathbf{A}\}$ and $|\mathbf{A}|$ stand for the trace and the determinant of the matrix \mathbf{A} , respectively. Equation (1) also defines the likelihood of the N pixels belonging to a region with known covariance matrix \mathbf{R} . Since in general \mathbf{R} is not known the likelihood function cannot be used directly. Therefore, we resort to the generalized likelihood ratio, by replacing the unknown covariance matrix with its ML estimate. It is easily shown that the estimated polarimetric covariance matrix is given by the sample covariance matrix estimated on the N -pixel region, so that the generalized likelihood function $L(\mathbf{x})$ of a homogeneous region of N pixels is [15]

$$L(\mathbf{x}) = \text{Max}_{\mathbf{R}} \{p(\mathbf{x})\} = \left(\frac{N}{\pi e} \right)^{MN} \frac{1}{\left| \sum_{n=1}^N \mathbf{x}_n \mathbf{x}_n^H \right|^N} \quad (2)$$

Following the maximum-likelihood approach, a ML split-merge test can be derived. This is required to test whether two regions A and B, with N_A and N_B pixels respectively, belong to the same statistic (and thus must be merged): hypothesis H_0 , or do not belong to the same statistic (and thus must be split): hypothesis H_1 . The generalized likelihood test for the two hypotheses yields

$$\lambda < \frac{\text{max}_{\mathbf{R}^{(0)}} \{p_{\mathbf{x}^{(A)}, \mathbf{x}^{(B)}}(\mathbf{x}^{(A)}, \mathbf{x}^{(B)} / \mathbf{R}^{(0)})\}}{\text{max}_{\mathbf{R}^{(A)}} \{p_{\mathbf{x}^{(A)}}(\mathbf{x}^{(A)} / \mathbf{R}^{(A)})\} \cdot \text{max}_{\mathbf{R}^{(B)}} \{p_{\mathbf{x}^{(B)}}(\mathbf{x}^{(B)} / \mathbf{R}^{(B)})\}} \quad (3)$$

where $\mathbf{R}^{(A)}$ and $\mathbf{R}^{(B)}$ are the covariance matrices of the two different regions in hypothesis H_1 , $\mathbf{R}^{(0)}$ is the common covariance matrix in the hypothesis H_0 , and λ is an appropriate threshold. By evaluating the maxima, it yields

$$\Lambda_M = \Lambda_M(N_A, N_B) = C^M \cdot \frac{|\Sigma^{(A)}|^{N_A} |\Sigma^{(B)}|^{N_B}}{|\Sigma|^N} > \lambda \quad (4)$$

having defined the random matrices

$$\begin{aligned} \Sigma^{(A)} &= \sum_{n=1}^{N_A} \mathbf{x}_n^{(A)} \mathbf{x}_n^{(A)H} \\ \Sigma^{(B)} &= \sum_{n=1}^{N_B} \mathbf{x}_n^{(B)} \mathbf{x}_n^{(B)H} \\ \Sigma &= \sum_{n=1}^N \mathbf{x}_n \mathbf{x}_n^H \\ &= \sum_{n=1}^{N_A} \mathbf{x}_n^{(A)} \mathbf{x}_n^{(A)H} + \sum_{n=1}^{N_B} \mathbf{x}_n^{(B)} \mathbf{x}_n^{(B)H} \\ &= \Sigma^{(A)} + \Sigma^{(B)} \end{aligned} \quad (5)$$

corresponding to the scaled sample correlation matrix in the regions A, B, and A + B. Moreover, we have set $N = N_A + N_B$ and the constant C is given by $C = C(N_A, N_B) = N^N / (N_A^{N_A} N_B^{N_B})$. The split-merge test in (4) is the basic step of both the global likelihood and the region-growing segmentation techniques proposed in [12] and [13]. After the derivation of the polarimetric test, in [12] and [13] only the global likelihood maximization via simulated annealing was implemented under the name of POLSEGANN. The split-merge approach, named polarimetric merge-using-moments (POL MUM), has presently been implemented into an effective segmentation routine and directly generalized for the multifrequency polarimetric case, by simply increasing the dimensionality of the input vector and replacing the number of polarimetric channels M with the sum of all available multifrequency polarimetric channels, $M_1 + M_2 = M$. Specifically, POL MUM iteratively tests adjacent segments for homogeneity and merges the mostly homogeneous set of adjacent segments. Only segments with polarimetric differences higher than a preassigned value can be merged, which yields a stop criterion to the algorithm. For this purpose, in [12], [13] the value of the test threshold was related to the probability of erroneously deciding to split segments with the same polarimetric properties, named probability of false alarm (P_{fa}). By defining the parameter

$$\rho_M = 1 - \frac{M^2 - 1}{6M} \left(\frac{1}{N_A} + \frac{1}{N_B} - \frac{1}{N} \right) \quad (6)$$

a first-order approximation in $\rho_M N$ can be found for the Laplace transform of $t = -\rho_M \ln \Lambda_M$ so that the asymptotic expression for the P_{fa} is

$$P_{fa} \cong 1 - \gamma(M^2/2, -\rho_M \ln \lambda) \quad (7)$$

where $\gamma(v, x)$ is the incomplete Gamma function of order v of x [16].

III. MODEL-BASED POLARIMETRIC SEGMENTATION

It is well known that in many cases (and specifically in the multifrequency polarimetric case under consideration) the covariance matrix of the polarimetric SAR images has a special known structure, which can be used to reduce the adaptivity losses. We consider the block diagonal matrix structure

$$\mathbf{R} = \begin{bmatrix} \mathbf{R}_1 & \mathbf{0} \\ \mathbf{0} & \mathbf{R}_2 \end{bmatrix} \quad (8)$$

where \mathbf{R}_1 and \mathbf{R}_2 are, respectively, M_1 -dimensional and M_2 -dimensional unknown polarimetric covariance matrices, with $M_1 + M_2 = M$. This is usually the case for multifrequency polarimetric SAR data, where the data at the different frequencies show a very low correlation, due to the different combination of the speckle phase contribution and, possibly, to the different scattering mechanism involved [1]. This is also the case for multitemporal polarimetric SAR images, collected with a temporal distance of many hours, as usual for the present earth-monitoring satellite sensors. Taking into account the specific structure of (8), and splitting the data vector for the single pixel as $\mathbf{x} = [\mathbf{x}_1^T, \mathbf{x}_2^T]^T = [x_1, \dots, x_{M_1}, x_1, \dots, x_{M_2}]^T$, the expression in (1) can be rewritten as

$$\begin{aligned} p(\mathbf{x}) &= \frac{1}{\pi^{MN} |\mathbf{R}_1|^N |\mathbf{R}_2|^N} \\ &\times \exp \left[-\text{Tr} \left\{ \begin{bmatrix} \mathbf{R}_1^{-1} & \mathbf{0} \\ \mathbf{0} & \mathbf{R}_2^{-1} \end{bmatrix} \right. \right. \\ &\times \sum_{n=1}^N \begin{bmatrix} \mathbf{x}_{1,n} \\ \mathbf{x}_{2,n} \end{bmatrix} \begin{bmatrix} \mathbf{x}_{1,n}^H & \mathbf{x}_{2,n}^H \end{bmatrix} \left. \right\} \right] \\ &= \frac{1}{\pi^{MN} |\mathbf{R}_1|^N |\mathbf{R}_2|^N} \\ &\times \exp \left[-\text{Tr} \left\{ \mathbf{R}_1^{-1} \sum_{n=1}^N \mathbf{x}_{1,n} \mathbf{x}_{1,n}^H \right\} \right. \\ &\left. - \text{Tr} \left\{ \mathbf{R}_2^{-1} \sum_{n=1}^N \mathbf{x}_{2,n} \mathbf{x}_{2,n}^H \right\} \right]. \end{aligned} \quad (9)$$

This expression can be exploited to derive a model-based segmentation technique for multifrequency polarimetric data. In fact, the estimates of the two reduced-size covariance matrices \mathbf{R}_1 and \mathbf{R}_2 are independent and correspond to the sample covariance matrix estimates on the N -pixel segment performed separately on the two sets of images (namely at the two frequencies). Therefore, the generalized likelihood for this case is given by

$$\begin{aligned} L(\mathbf{x}) &= \text{Max}_R \{p(\mathbf{x})\} \\ &= \left(\frac{N}{\pi e} \right)^{MN} \frac{1}{\left| \sum_{n=1}^N \mathbf{x}_{1n} \mathbf{x}_{2n}^H \right|^N \cdot \left| \sum_{n=1}^N \mathbf{x}_{1n} \mathbf{x}_{2n}^H \right|^N}. \end{aligned} \quad (10)$$

Under this assumption, the split-merge test obtained using the generalized likelihood test for the two hypotheses yields (11) (shown at the bottom of the page) where $\mathbf{R}_1(A), \mathbf{R}_1(B)$ and $\mathbf{R}_2(A), \mathbf{R}_2(B)$ are the covariance matrices of the two different regions in hypothesis \mathbf{H}_1 , $\mathbf{R}_{1(0)}$; $\mathbf{R}_{2(0)}$ is the common covariance matrix in the hypothesis \mathbf{H}_0 , and λ is an appropriate threshold. It is easy to show that this can be rewritten (as shown at the bottom of the page). By evaluating the maxima, it yields

$$\begin{aligned} \Phi_M &= \Phi_M(N_A, N_B) \\ &= C^M \cdot \frac{|\Sigma_1^{(A)}|^{N_A} |\Sigma_1^{(B)}|^{N_B}}{|\Sigma_1|^N} \cdot \frac{|\Sigma_2^{(A)}|^{N_A} |\Sigma_2^{(B)}|^{N_B}}{|\Sigma_2|^N} \\ &> \lambda \end{aligned} \quad (13)$$

where the following matrices have been defined:

$$\begin{aligned} \Sigma_1^{(A)} &= \sum_{n=1}^{N_A} \mathbf{x}_{1,n}^{(A)} \mathbf{x}_{1,n}^{(A)H} \\ \Sigma_1^{(B)} &= \sum_{n=1}^{N_B} \mathbf{x}_{1,n}^{(B)} \mathbf{x}_{1,n}^{(B)H} \\ \Sigma_2^{(A)} &= \sum_{n=1}^{N_A} \mathbf{x}_{2,n}^{(A)} \mathbf{x}_{2,n}^{(A)H} \\ \Sigma_2^{(B)} &= \sum_{n=1}^{N_B} \mathbf{x}_{2,n}^{(B)} \mathbf{x}_{2,n}^{(B)H} \\ \Sigma_1 &= \Sigma_1^{(A)} + \Sigma_1^{(B)} \\ \Sigma_2 &= \Sigma_2^{(A)} + \Sigma_2^{(B)} \end{aligned} \quad (14)$$

corresponding to the scaled sample M_1 - and M_2 -dimensional correlation matrices in the regions A, B, and A + B. It is inter-

$$\frac{\max_{\mathbf{R}_1^{(0)}, \mathbf{R}_2^{(0)}} \left\{ p_{\mathbf{x}^{(A)}, \mathbf{x}^{(B)}} \left(\mathbf{x}^{(A)}, \mathbf{x}^{(B)} / \mathbf{R}_1^{(0)}, \mathbf{R}_2^{(0)} \right) \right\}}{\max_{\mathbf{R}_1^{(A)}, \mathbf{R}_2^{(A)}} \left\{ p_{\mathbf{x}^{(A)}} \left(\mathbf{x}^{(A)} / \mathbf{R}_1^{(A)} \right) \right\} \cdot \max_{\mathbf{R}_1^{(B)}, \mathbf{R}_2^{(B)}} \left\{ p_{\mathbf{x}^{(B)}} \left(\mathbf{x}^{(B)} / \mathbf{R}_2^{(B)} \right) \right\}} > \lambda \quad (11)$$

$$\begin{aligned} &\frac{\max_{\mathbf{R}_1^{(0)}} \left\{ p_{\mathbf{x}_1^{(A)}, \mathbf{x}_1^{(B)}} \left(\mathbf{x}_1^{(A)}, \mathbf{x}_1^{(B)} / \mathbf{R}_1^{(0)} \right) \right\}}{\max_{\mathbf{R}_1^{(A)}} \left\{ p_{\mathbf{x}_1^{(A)}} \left(\mathbf{x}_1^{(A)} / \mathbf{R}_1^{(A)} \right) \right\} \cdot \max_{\mathbf{R}_1^{(B)}} \left\{ p_{\mathbf{x}_1^{(B)}} \left(\mathbf{x}_1^{(B)} / \mathbf{R}_1^{(B)} \right) \right\}} \\ &\cdot \frac{\max_{\mathbf{R}_2^{(0)}} \left\{ p_{\mathbf{x}_2^{(A)}, \mathbf{x}_2^{(B)}} \left(\mathbf{x}_2^{(A)}, \mathbf{x}_2^{(B)} / \mathbf{R}_2^{(0)} \right) \right\}}{\max_{\mathbf{R}_2^{(A)}} \left\{ p_{\mathbf{x}_2^{(A)}} \left(\mathbf{x}_2^{(A)} / \mathbf{R}_2^{(A)} \right) \right\} \cdot \max_{\mathbf{R}_2^{(B)}} \left\{ p_{\mathbf{x}_2^{(B)}} \left(\mathbf{x}_2^{(B)} / \mathbf{R}_2^{(B)} \right) \right\}} > \lambda \end{aligned} \quad (12)$$

esting to notice that, under the assumption above, the expression in (13) can be rewritten as

$$\begin{aligned}\Phi_M &= \Phi_M(N_A, N_B) = \Lambda_{M_1} \cdot \Lambda_{M_2} \\ &= \Lambda_{M_1}(N_A, N_B) \cdot \Lambda_{M_2}(N_A, N_B) > \lambda.\end{aligned}\quad (15)$$

Therefore, the test statistic in the model-based approach can be easily interpreted as the product of two test statistics obtained from the two independent portions of the pixel vector \mathbf{x} . Moreover, it is to be noted that only M_1 - and M_2 -dimensional covariance matrices must be estimated on the N -pixel region for the test in (13), whereas the application of the test in (4) would require the estimate of an $M = M_1 + M_2$ -dimensional covariance matrix on the same N -pixel region, which necessarily yields a larger estimation noise and, thus, a larger fluctuation of the test statistic. In consequence, this newly proposed model-based test is expected to yield better discrimination performance. The split-merge test in (13) is the basic step of a split-merge approach, named diagonal polarimetric merge-using-moments test (DPOL MUM) that has presently been implemented into an effective segmentation routine. The algorithm iteratively tests adjacent segments for homogeneity and merges the mostly homogeneous set of adjacent segments, following a similar approach to the one described in [1].

It is instructive to observe that the proposed discriminator in (13) can be used even when the covariance matrix decomposition in (8) does not apply; namely when the two sets of polarimetric images at different frequencies (or times) are not uncorrelated. Despite the test is derived under the assumption of a block diagonal structure for the covariance matrix, it shows no ill-conditioning when this assumption does not apply. In this latter case, the test in (13) has a lower discrimination capability than the full test in (4), but it still provides a robust discriminator with much lower estimation losses than (4). Therefore, in many cases (depending on the specific situation, but very likely for small window sizes) DPOL MUM still outperforms POL MUM, even when working with correlated sets of polarimetric SAR images.

IV. PERFORMANCE ANALYSIS OF THE OPTIMUM SPLIT-MERGE TEST

As expected from (14), the probability of false alarm (P_{fa}) depends on the number of pixels in the regions under test, as well as on the detection threshold λ . In the practical case it is useful to set the appropriate value of λ to achieve a desired value of P_{fa} ; therefore an analytic expression is required for the P_{fa} as a function of the above parameters. Unfortunately the pdf of the likelihood ratio Λ under hypothesis $H_0(\mathbf{R}^{(A)} = \mathbf{R}^{(B)} = \mathbf{R})$ is unknown, so that an exact expression for the P_{fa} is not available. To obtain an approximate expression, we proceed as follows.

First, the generic moment of the likelihood ratio Λ is evaluated under the hypothesis H_0 . When $\mathbf{R}^{(A)} = \mathbf{R}^{(B)} = \mathbf{R}$, it is shown in Appendix A that the h th moment of Λ_M is given by

$$\begin{aligned}\langle \Lambda_M^h \rangle &= C^{Mh} \frac{\tilde{\Gamma}_m(N)}{\tilde{\Gamma}_m[N(1+h)]} \\ &\times \frac{\tilde{\Gamma}_m[N_A(1+h)]}{\tilde{\Gamma}_m(N_A)} \frac{\tilde{\Gamma}_m[N_B(1+h)]}{\tilde{\Gamma}_m(N_B)}\end{aligned}\quad (16)$$

where the complex multivariate gamma function $\tilde{\Gamma}_m(a)$ corresponds to the integration over the space of the complex positive definite matrix \mathbf{A}

$$\begin{aligned}\tilde{\Gamma}_m(a) &\doteq \int_{\mathbf{A} > 0} \exp[-\text{Tr}(\mathbf{A})] \det \mathbf{A}^{a-m} d\mathbf{A} \\ &= \pi^{m(m-1)/2} \prod_{i=1}^m \Gamma[a - i + 1].\end{aligned}\quad (17)$$

Then, by using the expressions of the moments in (16) and defining the scaling parameter

$$\rho_M = 1 - \frac{M^2 - 1}{6M} \left(\frac{1}{N_A} + \frac{1}{N_B} - \frac{1}{N} \right) \quad (18)$$

a simple approximation can be found for the Laplace transform of $t = -\rho_M \ln \Lambda_M$ to the first order in $\rho_M N$ (see Appendix B), so that the asymptotic expression for the pdf is a Gamma distribution with order parameter $M^2/2$

$$p_t(t) \cong \frac{1}{\Gamma(M^2/2)} t^{M^2/2-1} e^{-t} + O(\rho_M^2 N^2). \quad (19)$$

Then, considering the test statistic in (15), we define the variable $\tau = -\rho_{M1} \ln \phi_M$ as

$$\begin{aligned}\tau &= -\rho_{M1} \ln \Phi_M = -\rho_{M1} \ln \Lambda_{M_1} - \rho_{M1} \ln \Lambda_{M_2} \\ &= t_A + \frac{\rho_{M1}}{\rho_{M2}} t_B\end{aligned}\quad (20)$$

where t_A and t_B are independent random variables, and ρ_{M1} and ρ_{M2} are obtained from (18) by replacing M with M_1 and M_2 , respectively. Based on the approximate pdf in (19), t_A and t_B follow a Gamma distribution with order parameters $M_1^2/2$ and $M_2^2/2$, respectively. Therefore, the approximate expression of the pdf of τ is given by (see Appendix B)

$$\begin{aligned}p_\tau(\tau) &= \sum_{k=1}^{M_1^2/2} A_k \frac{1}{\Gamma(k)} \tau^{k-1} e^{-\tau} \\ &+ \sum_{j=1}^{M_2^2/2} B_j \frac{1}{\Gamma(j)} \left(\frac{\rho_{M2}}{\rho_{M1}} \right)^j \tau^{j-1} e^{-\frac{\rho_{M2}}{\rho_{M1}} \tau}.\end{aligned}\quad (21)$$

For the special case of $M_1 = M_2 = M/2$, it yields $\tau = t_A + t_B$. Since both t_A and t_B have a Gamma pdf with the same mean and order, the pdf of τ is given itself by a Gamma pdf with order parameter $M_1^2 = M^2/4$, as

$$p_\tau(\tau) \cong \frac{1}{\Gamma(M^2/4)} \tau^{M^2/4-1} e^{-\tau}. \quad (22)$$

Finally, we observe that for the P_{fa} of the model-based split-merge test in (13) it yields

$$\begin{aligned}P_{fa} &= 1 - \Pr ob \{ \Phi_M > \lambda \} \\ &= 1 - \Pr ob \{ -\rho_{M1} \ln \Phi_M < -\rho_{M1} \ln \lambda \} \\ &= 1 - \int_0^{-\rho_{M1} \ln \lambda} p_\tau(\tau) d\tau.\end{aligned}\quad (23)$$

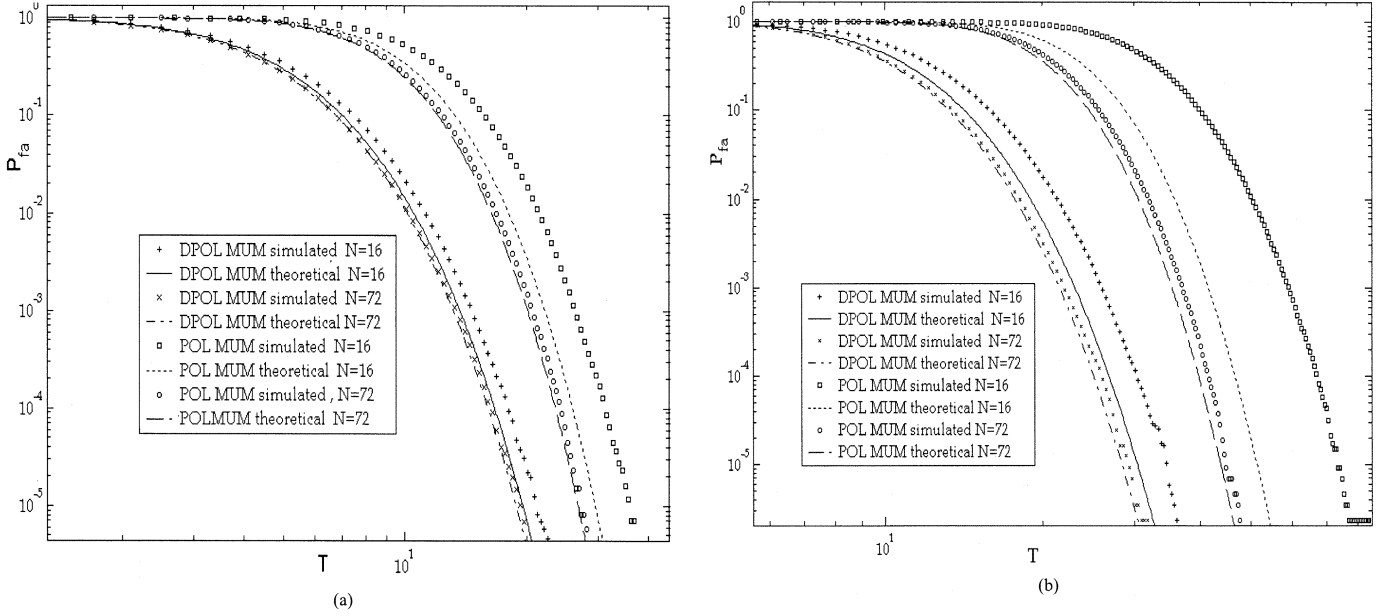


Fig. 1. Comparison of theoretical and simulated curves for the false-alarm probability of the different split-merge tests for different values of N , $N_A = N_B$, and (a) $M = 4$, (b) $M = 6$.

Therefore, the approximate expression of the P_{fa} is

$$P_{fa} = 1 - \sum_{k=1}^{M_1^2/2} A_k \gamma(k, -\rho_{M_1} \ln \lambda) - \sum_{j=1}^{M_2^2/2} B_j \gamma(j, -\rho_{M_2} \ln \lambda). \quad (24)$$

In the special case of $M_1 = M_2 = M/2$, using (22), it yields

$$P_{fa} \cong 1 - \gamma(M^2/4, -\rho_{M/2} \ln \lambda). \quad (25)$$

To validate the approximate closed-form expression in (24) and (25), a complete simulated analysis was carried out. This was obtained by generating random sets of complex pixel values with assigned multifrequency and polarimetric characteristics and applying the split-merge tests. For simplicity, the test in (7) and the model-based test in (13) are named after the corresponding region merging techniques, namely POL MUM and DPOL MUM, respectively. Fig. 1(a) and (b) shows the comparison of the theoretical results for the P_{fa} , as obtained from (7) and (25) respectively, to the results of the Monte Carlo simulations with 10^6 trials. The curves of P_{fa} as a function of the normalized threshold $T = -\log(\lambda)$ are reported for regions under test composed by $N = 72$ and $N = 16$ pixels, and a number of channels $M = 4$ in Fig. 1(a) and $M = 6$ in Fig. 1(b). The accuracy of the approximation is apparent in all the analyzed cases and for a wide range of P_{fa} values ($P_{fa} = 10^{-5}$ –1). The analytical plots depart significantly from the corresponding simulated curves only in the case of very small segments (i.e., small values of N), and this effect is slightly more evident for POL MUM than for DPOL MUM. This confirms our analytical results that are used inside the algorithm.

Unfortunately, a closed-form expression of the discrimination capability of the proposed split-merge tests is not available; thus, we resort to a Monte Carlo simulation. We define the probability of detection P_d as the probability of correctly

splitting two adjacent regions that have a multifrequency polarimetric difference. The performance are again obtained by a full Monte Carlo simulation that generates the complex pixel values of the two adjacent regions and feeds them into the tests to decide for splitting or merging. The receiver operating characteristics (ROCs), namely the plots of P_d versus P_{fa} , are reported in Fig. 2(a)–(d) for different values of $\mathbf{R}_1^{(A)}$, $\mathbf{R}_1^{(B)}$ and $\mathbf{R}_2^{(A)}$, $\mathbf{R}_2^{(B)}$. Specifically, the performances are assessed in the following four cases, which are representative of the possible operative conditions of two regions that have exactly the same polarimetric behavior on the first frequency and a little difference in the polarimetric characteristic of the second frequency:

- case (a)

$$\begin{aligned} \mathbf{R}_1^{(A)} = \mathbf{R}_1^{(B)} = \mathbf{R}_2^{(A)} &= \begin{bmatrix} 1 & 0.3 \\ 0.3 & 1 \end{bmatrix} \\ \mathbf{R}_2^{(B)} &= \begin{bmatrix} 1 & 0.85 \\ 0.85 & 1 \end{bmatrix} \end{aligned} \quad (26)$$

- case (b)

$$\begin{aligned} \mathbf{R}_1^{(A)} = \mathbf{R}_1^{(B)} = \mathbf{R}_2^{(A)} &= \begin{bmatrix} 1 & 0 \\ 0 & 1 \end{bmatrix} \\ \mathbf{R}_2^{(B)} &= \begin{bmatrix} 1 & 0.9 \\ 0.9 & 1 \end{bmatrix} \end{aligned} \quad (27)$$

- case (c)

$$\begin{aligned} \mathbf{R}_1^{(A)} = \mathbf{R}_1^{(B)} = \mathbf{R}_2^{(A)} &= \begin{bmatrix} 1 & 0.75 \\ 0.75 & 1 \end{bmatrix} \\ \mathbf{R}_2^{(B)} &= \begin{bmatrix} 5 & 0.85 \\ 0.85 & 5 \end{bmatrix} \end{aligned} \quad (28)$$

- case (d)

$$\begin{aligned} \mathbf{R}_1^{(A)} = \mathbf{R}_1^{(B)} = \mathbf{R}_2^{(A)} &= \begin{bmatrix} 1 & 0.75 \\ 0.75 & 1 \end{bmatrix} \\ \mathbf{R}_2^{(B)} &= \begin{bmatrix} 1.5 & 0.85 \\ 0.85 & 1.5 \end{bmatrix} \end{aligned} \quad (29)$$

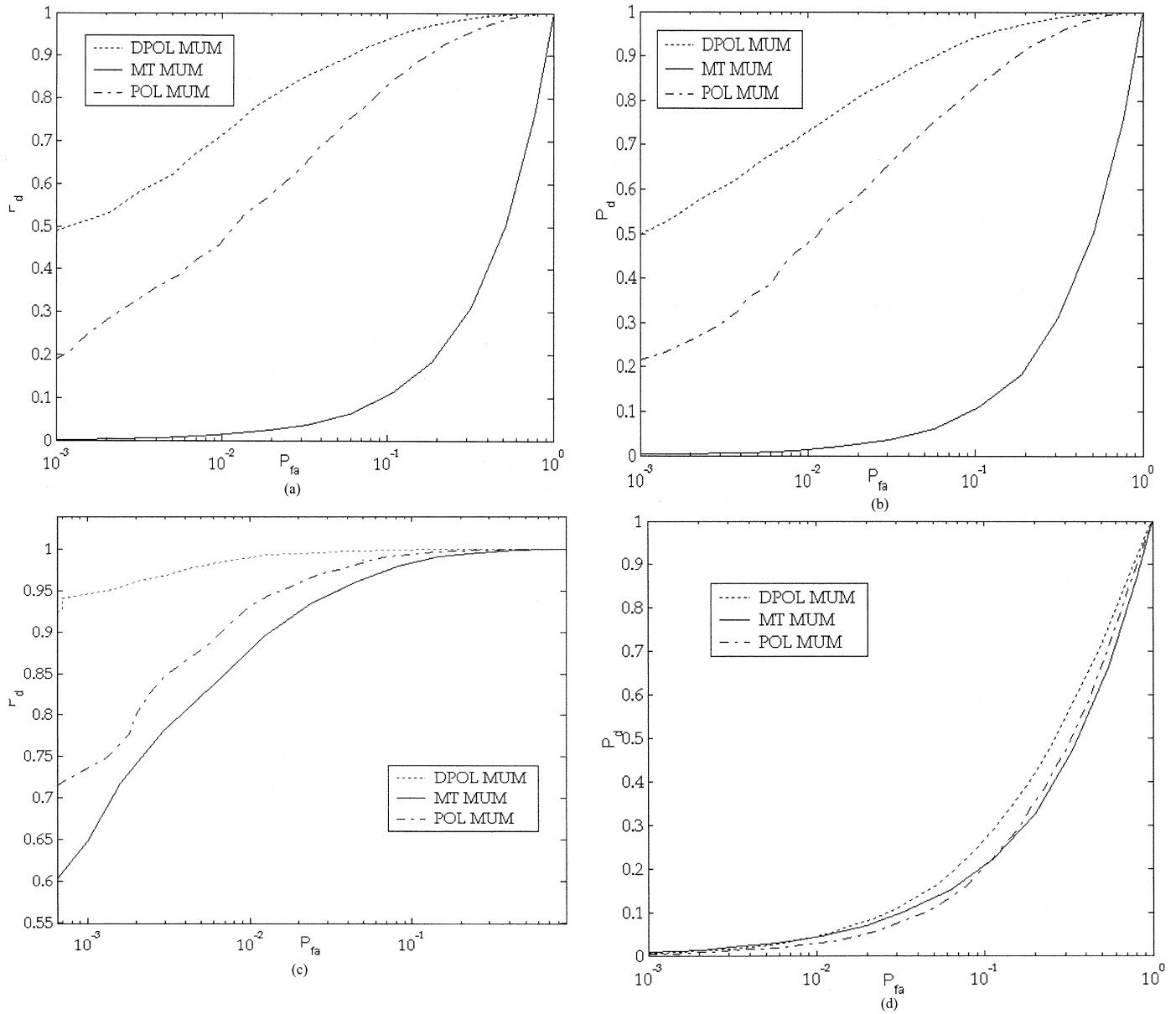


Fig. 2. Simulated ROCs for the proposed split-merge test for $N = 16$, $N_A = N_B$, and $\mathbf{R}_1^{(A)}$, $\mathbf{R}_1^{(B)}$, $\mathbf{R}_2^{(A)}$, $\mathbf{R}_2^{(B)}$ given (a) in (28), (b) in (29), (c) in (30), and (d) in (31).

Fig. 2(a)–(d) shows the ROC curves obtained for the POL MUM and DPOL MUM tests, when applied to two adjacent regions of $N = 16$ pixels. The performance of the multitemporal merge-using-moments test (MT MUM) is also reported for comparison [17], [18], as such split-merge test has been derived following the approach of (4) and assuming $\mathbf{R}^{(A)}$ and $\mathbf{R}^{(B)}$ fully diagonal. As expected this latter test does not make use of the correlation property of the different channels. The following is apparent from Fig. 2(a)–(d).

- 1) Polarimetric MUM-based tests always outperform the MT MUM as they fully exploit the information contained in the polarimetric covariance matrix.
- 2) Performance improvement is large when the mean reflectivity of region B at the second frequency is unchanged, while only the correlation between the two polarimetric channels changes, cases (a) and (b).

- 3) DPOL MUM always outperforms the POL MUM as it is less affected by estimation errors, while having the same discrimination capability.
- 4) Strong reflectivity change is well detected by all the three tests, case (c), and the DPOL MUM still yields the best performance.
- 5) In the worst case, namely the case of presence of a small reflectivity change together with only a small variation in the correlation coefficient, case (d), the three tests show similar performance.

These considerations clearly show that a neat theoretical improvement is available when properly exploiting the considered model with DPOL MUM. Various conditions for the two regions have been considered that always report for DPOL MUM better discrimination capability than MT MUM and a higher sensitivity than the full POL MUM, being affected by a lower estima-

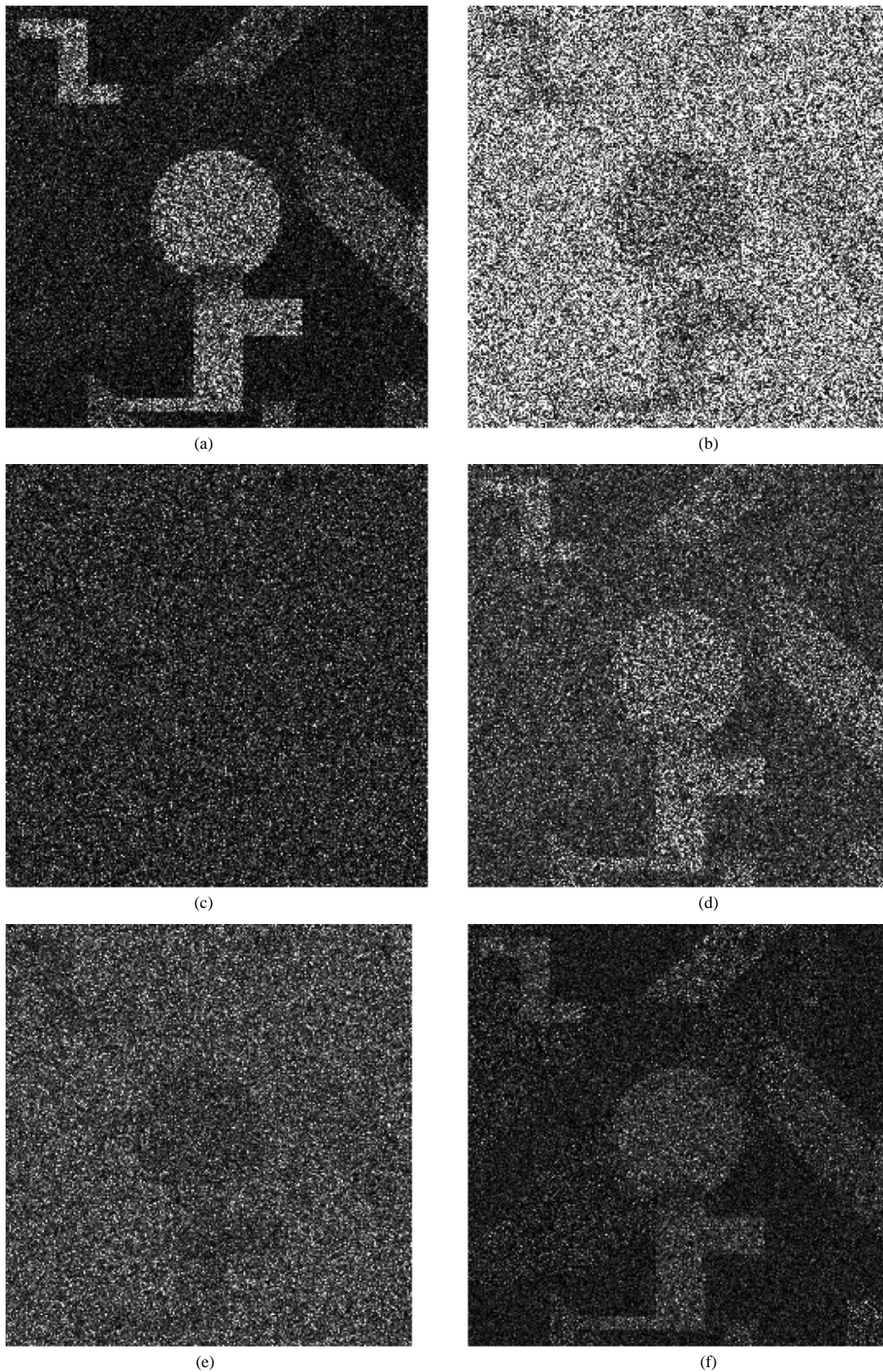


Fig. 3. Example of synthetic images used to test the different segmentation algorithms. (a)–(c) Intensities of the three considered channels. (d)–(f) Modulus of the cross products of the different channels.

tion error. Obviously, this improvement is only available when the actual covariance matrix of the data is really block diagonal,

which is certainly the case for the considered multifrequency images, as well as for the case of multitemporal images [18].

TABLE I
COVARIANCE MATRICES FOR THE SYNTHETIC IMAGES (a) CLASS 1, (b) CLASS 2, (c) CLASS 3, (d) CLASS 4, (e) CLASS 5, (f) CLASS 6, AND (g) CLASS 7

0,1846	0	0	0,3946	0,3663	0,3425
0	1,5704	0	0,3663	1,3604	0,1476
0	0	0,345	0,3425	0,1476	0,345
(a)			(b)		
0,3144	0,4038	0	0,2256	0,235	0
0,4038	1,4406	0	0,235	1,5294	0
0	0	0,345	0	0	0,345
(c)			(d)		
0,499	0,3958+0,3958i	0,1317+0,0658i	0,8359	0,6837	0,0563
0,3958-0,3958i	1,256	0,0415+0,0207i	0,6837	0,9191	0,0967
0,1317-0,0658i	0,0415-0,0207i	0,345	0,0563	0,0967	0,345
(e)			(f)		
			0,2448	0,1824	0,2165
			0,1824	1,5102	0,0872
			0,2165	0,0872	0,345
			(g)		

The performance of the region growing segmentation technique based on the proposed test is analyzed in the following section.

V. SEGMENTATION COMPARATIVE PERFORMANCE ANALYSIS

In this section, we analyze the results obtained by applying the MT MUM, POL MUM, and DPOL MUM algorithms on a set of simulated synthetic images. To emulate the case of six channels of dual frequency polarimetric SAR images, we considered a set of six images ($M = 6$), characterized by a block diagonal covariance matrix. The size of each block is $M_1 = M_2 = 3$, and for simplicity of simulation the two blocks are considered identical. Fig. 3(a)–(c) shows the intensity (square modulus) of the three channels, while Fig. 3(d)–(f) shows the modulus of the cross products of the considered channels. The images are obtained from the same pattern of regions, composed of seven different classes, each one characterized by a different covariance matrix. The seven covariance matrices are reported in Table I. From the analysis of the different images and covariance matrices, we make the following observations.

- All the covariance matrices have the same trace, and this means that the average intensity of the three channels is the same for all classes; moreover, the intensity of the second channel is definitely higher than the intensities of the other two for all the classes.
- The covariance matrices of classes 1, 3, and 4 have the same determinant, which that is equal to 0.1; moreover, the determinant of the covariance matrix of class 6 is equal to 0.1005.
- Classes 4 and 7 show very similar intensities for the three channels. Thus, a segmentation scheme based only on the intensities is very likely to confuse the two classes, while the addition of the information about the phase relationships among the two channels is expected to increase the discrimination capability of the segmentation procedure.

We now compare the results obtained by running the different segmentation routines on the synthetic data. Segmenta-

tion is controlled by the desired value of P_{fa} that sets the fusion threshold. By reducing the value of this parameter the segmentation procedure finds a solution with larger regions, and thus less ragged boundaries. We choose the value of P_{fa} that maximizes the probability of correct classification against the test pattern, which largely depends on the characteristics of the images and on the number of looks. In this case, for the emulated single-look images we found the best classification performance for $P_{fa} = 10^{-4}$. We generated ten independent sets of synthetic images, and we performed segmentation with all three algorithms on each set. Fig. 4 shows the results for one of the considered sets, together with the original pattern. In particular, Fig. 4(a) shows the segmentation obtained running the MT MUM technique on the intensities of the different channels, while Fig. 4(b) shows the segmentation obtained with POL MUM, and Fig. 4(c) the segmentation obtained with the newly conceived DPOL MUM technique. The following comments apply.

- When comparing Fig. 4(a)–(c), it is apparent that in the latter case the identification of the region borders is extremely more accurate. This is especially true for the big region in the upper left part of the image: its circular border is not clearly defined in Fig. 4(a). Moreover, some homogeneous regions have been oversegmented by MT MUM, and some others completely disappeared. In particular, the diagonal strip from the lower left to the upper right part of the image has been completely merged to the surrounding region. This is consistent with our expectations, since the strip belongs to class 4, while the surrounding region belongs to class 7. As previously noticed, the two classes have very similar intensities; thus, they are merged. On the contrary, when using the full covariance matrix to perform segmentation (namely when using POL MUM and DPOL MUM) the differences between the two regions are more evident, and thus they are not merged.
- The comment above does not apply to the comparison between POL MUM and DPOL MUM. In fact, both routines

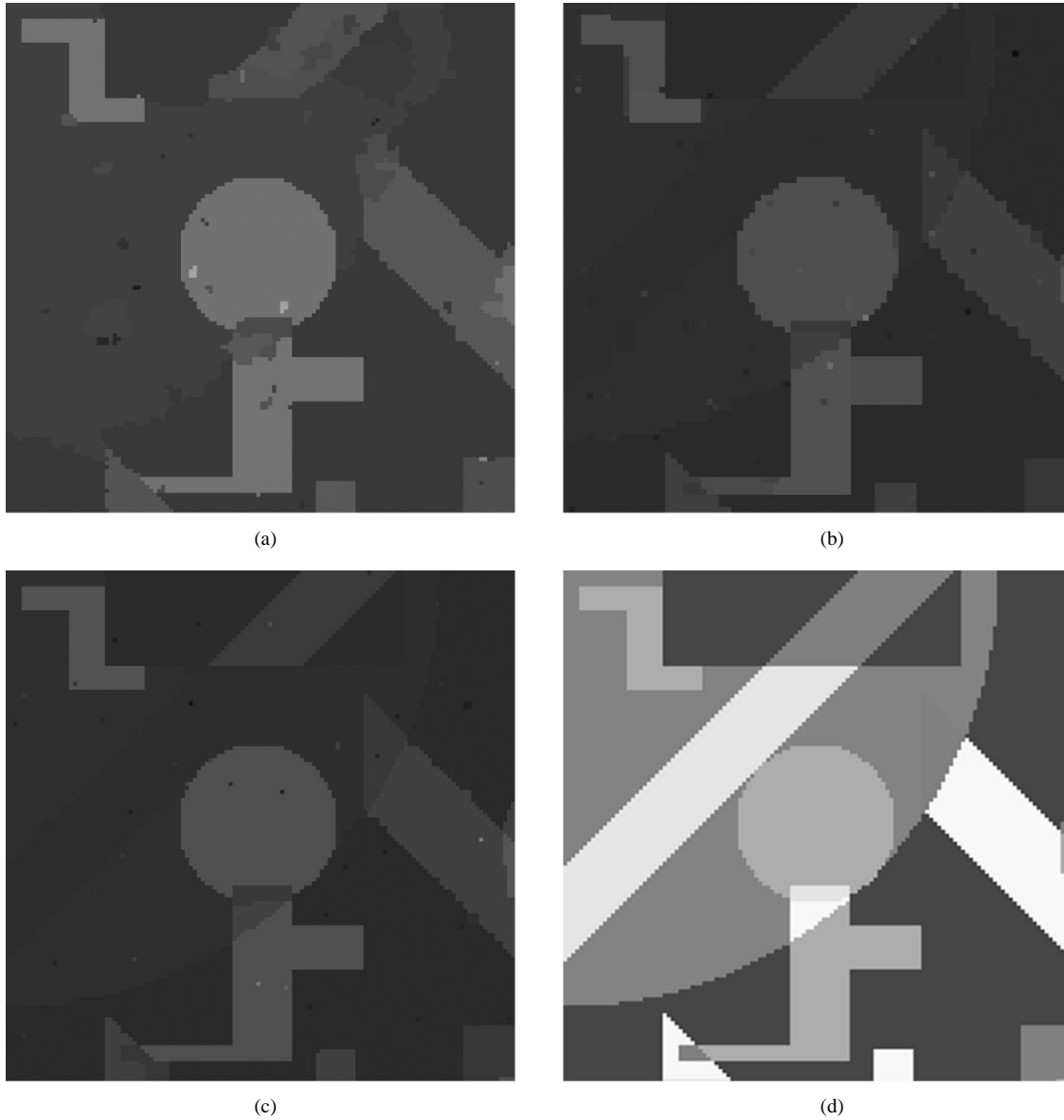


Fig. 4. Segmentation output for $P_{fa} = 10^{-4}$ having applied the different routines on the images in Fig. 3. (a) MT MUM. (b) POL MUM. (c) DPOL MUM. (d) Original pattern showing the different regions.

exploit the polarimetric properties of the input dataset, and consequently both perform better than MT MUM. However, after the application of POL MUM some regions are still oversegmented; moreover, the region borders are less smoothed or reconstructed less accurately than those obtained with DPOL MUM. This is a consequence of the initial decomposition of the input images in square regions of 3×3 pixels (rather than 2×2 , as in DPOL MUM), which was required to allow the estimation of all the elements of the 6×6 covariance matrix.

To provide a quantitative measure of the quality of the different segmentation schemes, we applied the same classifier to the regions identified with the different techniques. In particular, we use a ML supervised classifier, based on the statistical model in (1), assuming that the polarimetric characteristics of the seven classes $c = 1, \dots, 7$ are known (i.e., their covariance matrix \mathbf{R}_c is known). Thus, the generic segment of N pixels is assigned to

class \hat{c} that maximizes the corresponding likelihood

$$\begin{aligned} \hat{c} &= \arg \min_c \left\{ \ln(|\mathbf{R}_c|) + \text{Tr} \left[\mathbf{R}_c^{-1} \frac{1}{N} \sum_{n=1}^N \mathbf{x}_n \mathbf{x}_n^H \right] \right\} \\ &= \arg \min_c \left\{ \ln(|\mathbf{R}_c|) + \text{Tr} \left[\mathbf{R}_c^{-1} \hat{\mathbf{R}} \right] \right\} \end{aligned} \quad (30)$$

where $\hat{\mathbf{R}}$ is the sample covariance matrix estimated on the whole segment.

The classified images are reported in Fig. 5(a)–(c) for the case of MT MUM, POL MUM and DPOL MUM respectively, while the original pattern of the different classes is reported in Fig. 5(d) for purpose of comparison. To compare the performance of the classifier for the different classes, in Table II(a)–(c) we show the average confusion matrix over the ten sets of images for the different segmentation techniques. In particular, Table II(a) refers to the classification of the regions identified with the MT MUM

TABLE II
AVERAGE CONFUSION MATRIX RESULTING FROM THE CLASSIFICATION OF THE REGIONS OBTAINED WITH THE DIFFERENT SEGMENTATION TECHNIQUES.
(a) MT MUM, (b) POL MUM, AND (c) DPOL MUM

Original class	Assigned class							
		Class 1	Class 2	Class 3	Class 4	Class 5	Class 6	Class 7
	Class 1	96,4%	0,2%	0,0%	0,1%	0,3%	0,0%	3,0%
	Class 2	1,7%	66,1%	0,0%	0,3%	8,0%	0,2%	23,7%
	Class 3	0,7%	0,0%	54,4%	0,0%	40,9%	3,6%	0,3%
	Class 4	0,2%	0,2%	0,0%	0,2%	0,0%	0,0%	99,3%
	Class 5	0,9%	0,0%	0,5%	0,0%	95,8%	1,6%	1,2%
	Class 6	0,0%	0,1%	0,0%	0,0%	0,4%	99,3%	0,1%
	Class 7	5,8%	0,1%	0,0%	0,0%	0,1%	0,1%	93,8%

(a)

Original class	Assigned class							
		Class 1	Class 2	Class 3	Class 4	Class 5	Class 6	Class 7
	Class 1	98,1%	0,0%	0,1%	0,1%	0,4%	0,6%	0,6%
	Class 2	2,5%	90,5%	0,2%	0,0%	1,8%	0,3%	4,7%
	Class 3	0,0%	0,0%	79,9%	0,0%	6,5%	13,5%	0,0%
	Class 4	0,1%	0,0%	0,0%	96,9%	0,0%	0,1%	2,8%
	Class 5	4,4%	0,0%	1,0%	0,4%	93,1%	0,9%	0,2%
	Class 6	0,2%	0,0%	1,2%	0,2%	0,4%	97,3%	0,6%
	Class 7	1,9%	0,0%	0,8%	3,5%	0,0%	1,0%	92,7%

(b)

Original class	Assigned class							
		Class 1	Class 2	Class 3	Class 4	Class 5	Class 6	Class 7
	Class 1	99,7%	0,0%	0,0%	0,1%	0,1%	0,0%	0,1%
	Class 2	0,0%	99,6%	0,1%	0,0%	0,0%	0,1%	0,2%
	Class 3	1,2%	0,0%	78,9%	0,0%	16,1%	3,8%	0,0%
	Class 4	0,1%	0,0%	0,1%	98,6%	0,0%	0,0%	1,2%
	Class 5	1,0%	0,0%	0,3%	0,1%	98,2%	0,4%	0,0%
	Class 6	0,0%	0,0%	0,1%	0,0%	0,2%	99,7%	0,0%
	Class 7	0,5%	0,0%	0,0%	1,2%	0,0%	0,0%	98,2%

(c)

segmentation routine, while Table II(b) refers to the POL MUM routine, and Table II(c) refers to the DPOL MUM routine. On each row we can read the percentage of pixels belonging to a given class that has been assigned to any of the considered classes. Thus, the elements of the diagonal represent the percentage of correctly classified pixels for each class. A few considerations apply from the comparison of the three confusion matrices.

- Class 4 is completely misclassified when considering the segmentation obtained with MT MUM. This is of course a consequence of the fact—noticed previously—that the region belonging to that class is almost totally merged with the surrounding region.
- A nonnegligible percentage of the pixels of class 3 is misclassified by all three techniques. This is a consequence of the limited number of pixels belonging to this class, which causes the classification performance to be very sensitive to small variations in the shape of the region borders.
- The percentage of correctly classified pixels operating with DPOL MUM is generally higher than with POL MUM. The improvement is more evident for classes 2, 5, and 7, where the percentage of correctly classified pixels is increased, respectively, from 90.5% to 99.6% (class 2), from 93.1% to 98.2% (class 5), and from 92.7% to 98.2% (class 7). This is a consequence of a more accurate identification of the re-

TABLE III
AVERAGE PROBABILITY OF CORRECT CLASSIFICATION FOR THE DIFFERENT SEGMENTATION TECHNIQUES

MT MUM	POL MUM	DPOL MUM
72.3%	92.7%	96.1%

gion borders, and it is more evident for these classes since their borders are not vertical or horizontal lines; thus, they are more difficult to be identified correctly by the segmentation algorithm.

Finally, to provide a global measure of the classification accuracy achievable with the different techniques, we evaluate the average probability of correct classification (P_{cor}) for the whole image. This is evaluated by averaging the probabilities of correct classification for the different classes, namely by averaging the elements of the diagonal of the confusion matrix. The values of P_{cor} for the different segmentation algorithms, reported in Table III, confirm the results of the simulated analysis. In particular, it is apparent that the use of the polarimetric information dramatically increases the accuracy in the identification of the different regions

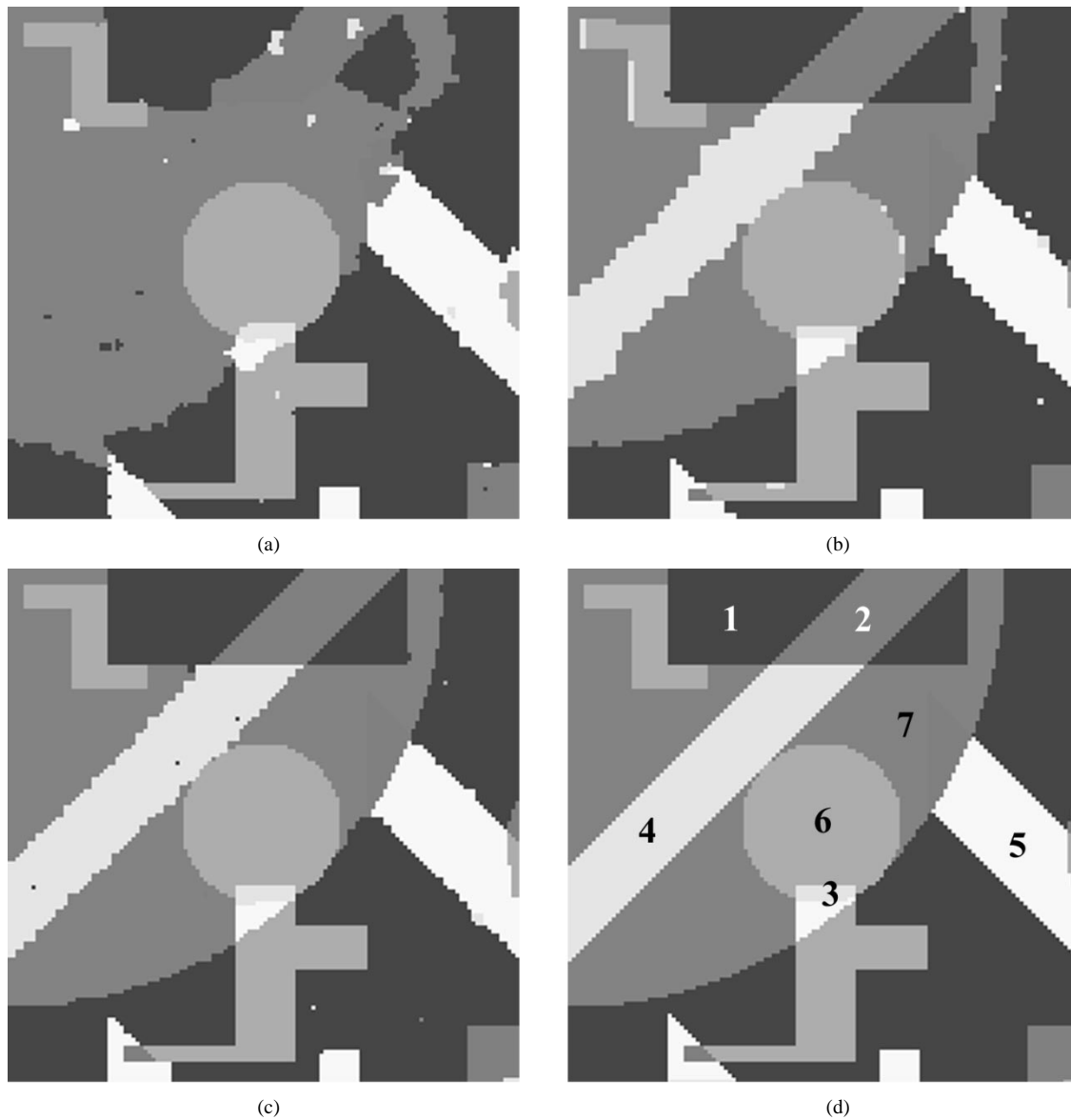


Fig. 5. Classification output applying the ML classifier over the segments shown in Fig. 4. (a) MT MUM. (b) POL MUM. (c) DPOL MUM. (d) Original pattern showing the different classes.

(P_{cor} raises from 72.3% for MT MUM to more than 92% for the polarimetric segmentation routines). Moreover, the exploitation of the *a priori* information available about the structure of the covariance matrix provides a further increase in the identification accuracy, yielding an average probability of correct classification of 96%.

VI. APPLICATION TO A SAR IMAGE OF URBAN AREAS

To show the effectiveness of the proposed segmentation technique, we consider a set of SIR-C polarimetric images of the town of Pavia, in northern Italy. The set is composed of the following images:

- C-band HH, VV, HV, and VH channels;
- L-band HH, VV, HV, and VH channels.

The images were collected on April 14, 1994 under mode 16 (multilook complex, quad pol), and their spatial resolution is 25 m in azimuth and 25 m in range. The urban environment is es-

pecially interesting for the multifrequency polarimetric images since a small area contains a very high variety of different behaviors both in frequency and polarization, and a high sensitivity to these differences is essential to extract the most information from the remotely sensed data [19].

For simplicity, in our analysis we only consider the two like-polarized channels. The intensities of the different channels are reported in Fig. 6(a)–(d). In particular, Fig. 6(a) and (b) shows the C-band HH and VV channels respectively, while Fig. 6(c) and (d) shows the L-band HH and VV channels, respectively. A partial knowledge of the ground truth is available for the considered dataset, composed of three different classes: 1) water, 2) agricultural area, and 3) built up area. The ground truth was extracted from the technical regional map of the area, and validated with *in situ* observations. The whole ground truth was split into a training set and a test set, respectively, used to estimate the covariance matrix of the different classes and to evaluate the classification results. The training set is reported in Fig.

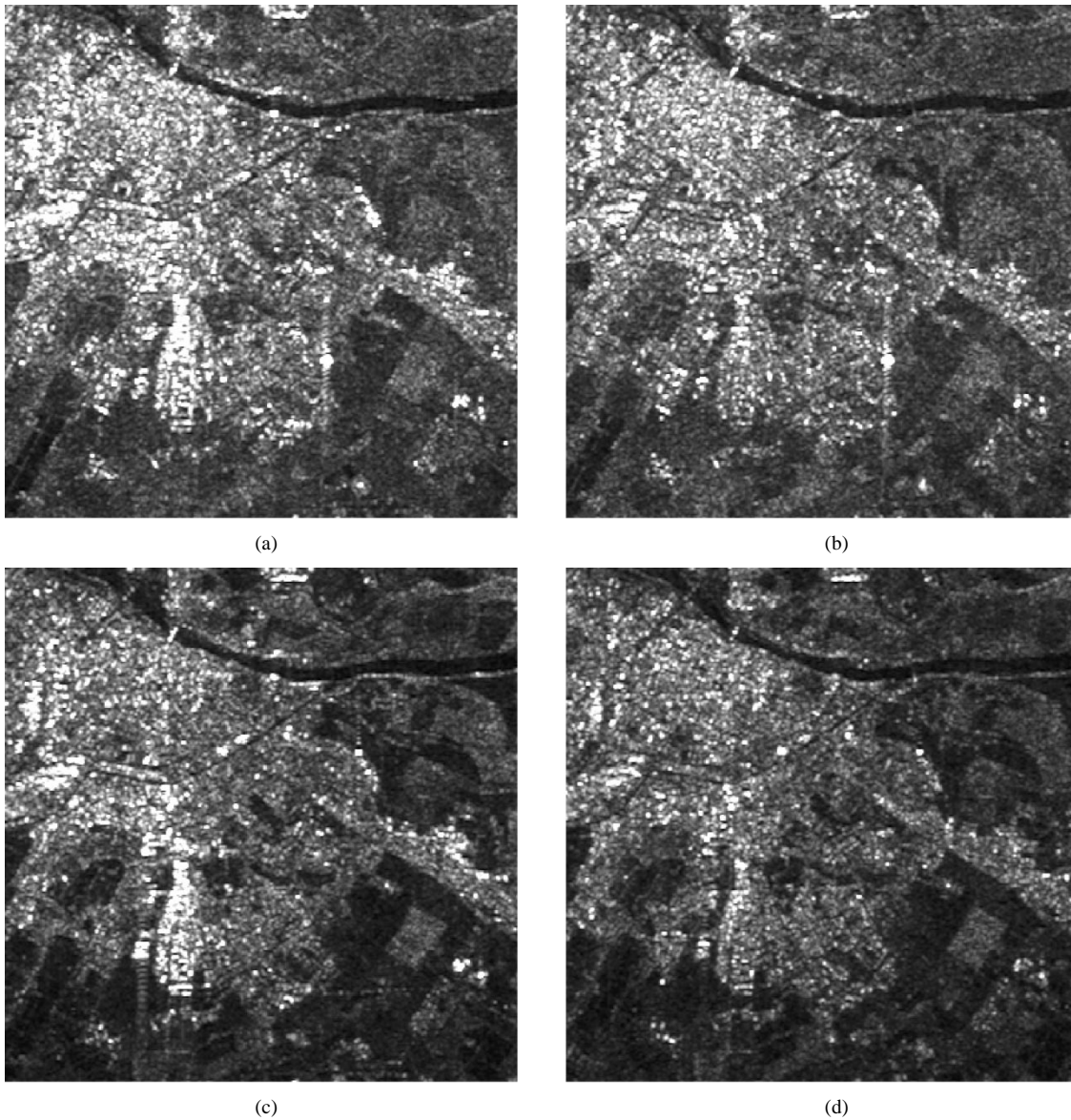


Fig. 6. Original intensity SIR-C images. (a) C-band HH polarization. (b) C-band VV polarization. (c) L-band HH polarization. (d) L-band VV polarization.

7(a), while the test set is reported in Fig. 7(b). The average polarimetric characteristics of the three classes, measured on the training set, are reported in Table IV, which is used as input to the ML classifier.

We apply the different segmentation routines on the considered data, for different values of the probability of false alarm and of the size of the initial segments. This latter parameter defines the size of the initial tessellation of the image from which the region merging technique starts its operation. Specifically, we consider values of P_{fa} from 10^{-2} to 10^{-50} , and region sizes from 2×2 pixels to 4×4 pixels. We then apply the ML classifier derived in the previous section to each one of the segmented images, and then we select the values of P_{fa} and of the region size that yield the highest average probability of correct classification (P_{cor}). The best segmentations according to this criterion are as follows:

- $P_{fa} = 10^{-14}$ and initial region size of 2×2 pixels for MT MUM;

- $P_{fa} = 10^{-15}$ and initial region size of 2×2 pixels for POL MUM;
- $P_{fa} = 10^{-50}$ and initial region size of 2×2 pixels for DPOL MUM.

The corresponding segmented images are reported in Fig. 8(a)–(c). Specifically, Fig. 8(a) shows the segmentation obtained with MT MUM. Fig. 8(b) shows the segmentation obtained with POL MUM, and Fig. 8(c) shows the segmentation obtained with DPOL MUM. From the comparison of the three images, it is apparent that, despite the lower value of P_{fa} , the DPOL MUM routine tends to identify a higher number of homogeneous regions, and it tends to identify more accurately the borders. This is a consequence of 1) the increased amount of used information with respect to MT MUM, and 2) the lower level of noise in the estimation of the covariance matrix with respect to POL MUM. As mentioned, the latter is a consequence of the *a priori* assumption of a block diagonal covariance matrix, which implies that only a reduced number of elements of the covariance matrix must be estimated from

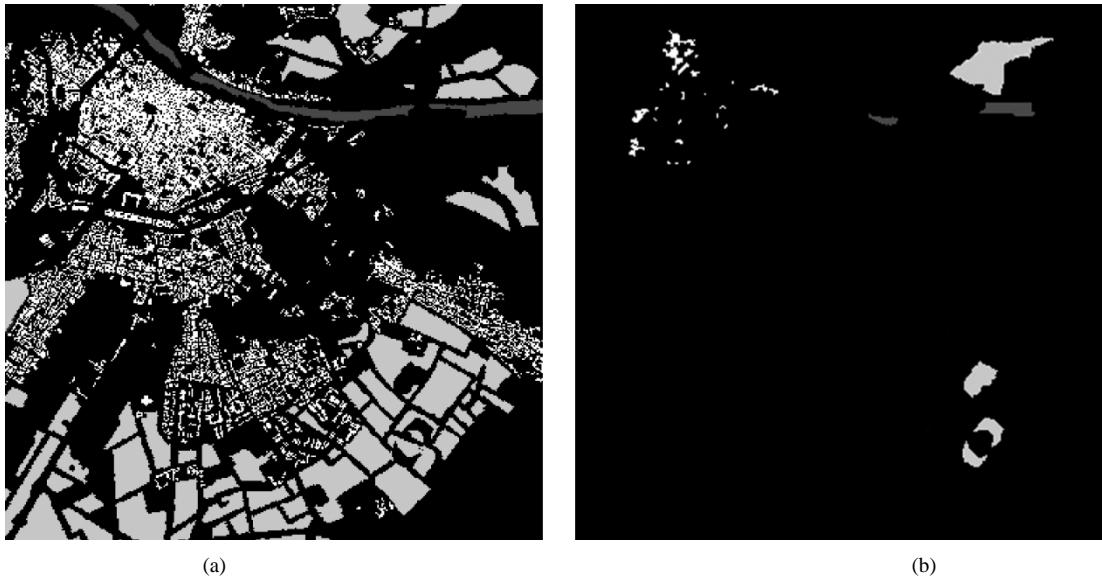


Fig. 7. (a) Test set and (b) training set for the images in Fig. 6. Dark gray: water (class 1). Light gray: agricultural areas (class 2). White: built-up areas (class 3).

TABLE IV
ESTIMATED COVARIANCE MATRIX FOR THE PIXELS OF THE TRAINING SET. (a) CLASS 1 (WATER), (b) CLASS 2 (AGRICULTURAL AREAS), AND (c) CLASS 3 (BUILT-UP AREAS)

0.016	0.0044- 0.0002i	0	0	0.0712	0.0373+ 0.0015i	0	0
0.0044+ 0.0002i	0.0207	0	0	0.0373- 0.0015i	0.0679	0	0
0	0	0.0118	0.0051+ 0.0008i	0	0	0.0366	0.0169+ 0.0022i
0	0	0.0051- 0.0008i	0.0116	0	0	0.0169- 0.002i	0.0311

(a)

0.6961	0.0848- 0.095i	0	0
0.0848+ 0.095i	0.6263	0	0
0	0	0.425	-0.0069- 0.0484i
0	0	-0.0069+ 0.0484i	0.3113

(b)

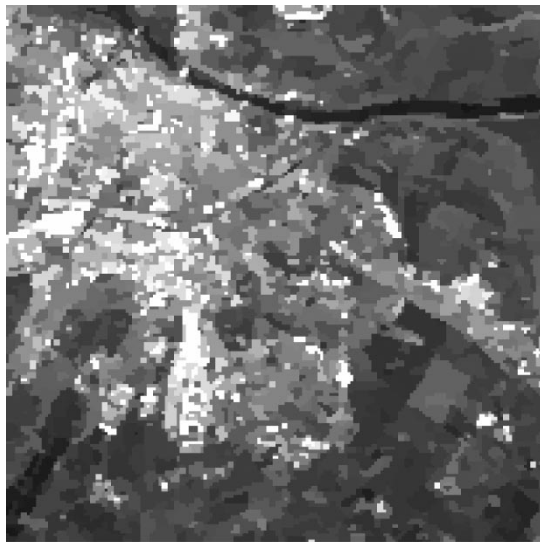
(c)

the data. Unfortunately, the higher polarimetric sensitivity also yields isolated pixels that are not merged as expected; however, this does not degrade globally the classification performance.

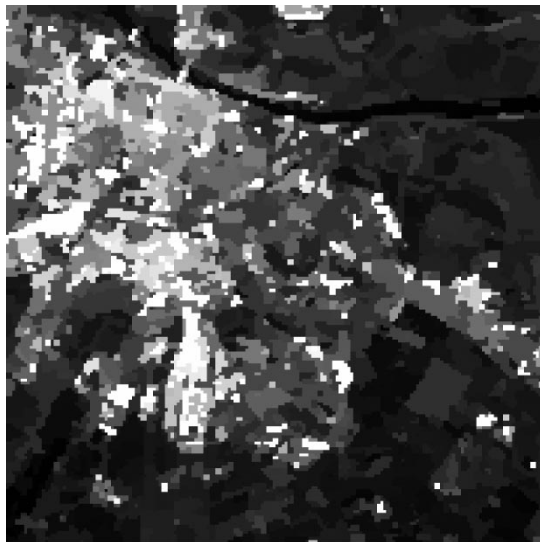
The classification is performed on the original images, by classifying together all the pixels in each of the homogeneous regions identified by each of the segmentation techniques. The same ML polarimetric classifier is used for the classifications, independently of the used segmentation technique. The resulting classified images are shown in Fig. 9(a)–(c), respectively, for MT MUM, POL MUM, and DPOL MUM. The values of the average probability of correct classification in the three cases are reported in Table V. As apparent, the higher accuracy provided by DPOL MUM in the identification of the borders of the homogeneous segments results in an increased accuracy in the classification results, with the average probability of correct classification that is increased from 80.7% for POL MUM to 82.9% for DPOL

MUM, thus showing the effectiveness of the proposed algorithm for the practical application.

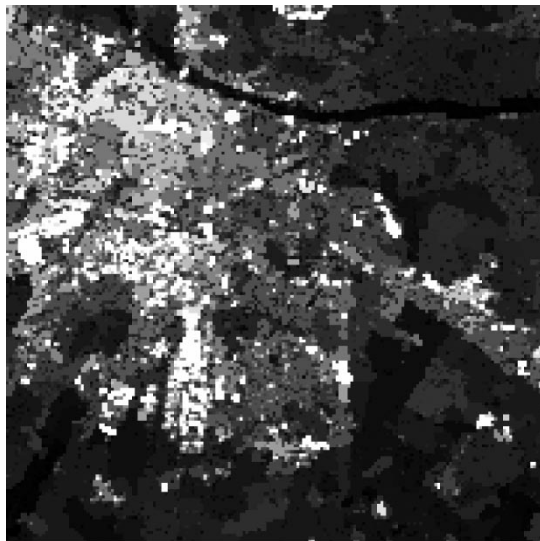
Despite the speckle at different bands being theoretically independent [20], SAR images of areas different from the considered urban environment have been found to show some level of correlation even at largely different frequencies. This is the case considered in [21], where the little correlations in the cross-covariance matrix are exploited to refine a preliminary classification for forest areas. For the considerations made at the end of Section 3, it is apparent that the proposed DPOL MUM would still perform effectively on such images, yielding a robust segmentation with the highest possible geometric resolution. In fact, on the small window of the segmentation technique, it would be impossible to exploit the small correlation values, while the large reduction of the covariance estimation uncertainty has a positive effect on the accuracy of segmentation.



(a)

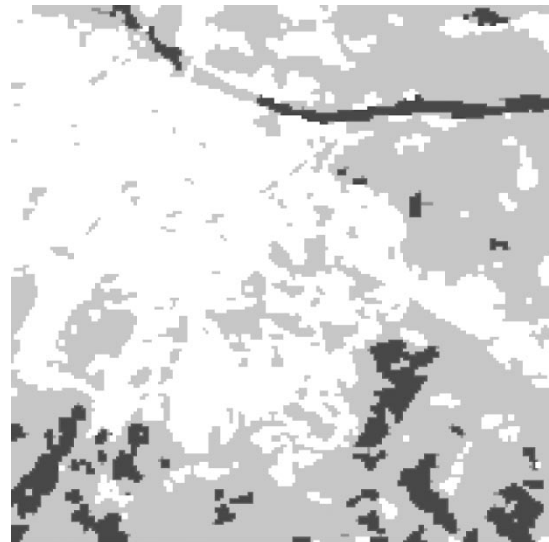


(b)

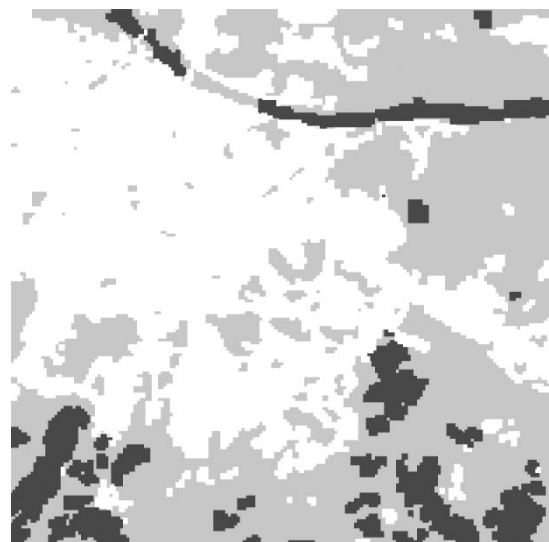


(c)

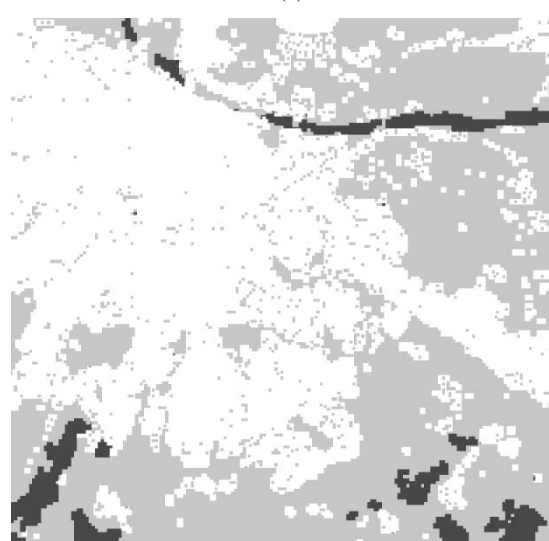
Fig. 8. Segmentation results after the application of the different segmentation algorithms on the SIR-C dataset. (a) MT MUM. (b) POL MUM. (c) DPOL MUM.



(a)



(b)



(c)

Fig. 9. Classification results applying the ML classifier on the segmentations in Fig. 8. (a) MT MUM. (b) POL MUM. (c) DPOL MUM.

TABLE V
AVERAGE PROBABILITY OF CORRECT CLASSIFICATION FOR THE DIFFERENT
SEGMENTATION TECHNIQUES

MT MUM	POL MUM	DPOL MUM
80.6%	80.7%	82.9%

VII. CONCLUSION

An effective technique, DPOL MUM, has been proposed for the segmentation of multifrequency polarimetric SAR images, which exploits the characteristic block diagonal structure of their covariance matrix. This technique is based on the newly introduced split–merge test that has a reduced fluctuation error than the straight extension of the polarimetric test (POL MUM) and can yield a more accurate segmentation. An approximate analytic expression for the false-alarm probability of this test has been derived in closed form to be used inside the algorithm to control the fusion of adjacent regions and the stopping criterion. A full Monte Carlo simulation was used both to validate the analytical results and to assess the discrimination capability of the new test, which proved to yield better performance than both the tests of POL MUM and the MT MUM scheme that does not use the correlation properties. Similarly, a ML classification performed after the segmentation of a set of simulated images showed that segmenting with DPOL MUM yields a largely higher probability of correct classification than segmenting with both POL MUM and MT MUM. Moreover, the application of DPOL MUM to an image of urban and suburban environment that is especially affected by frequency and polarization differences shows an improvement of classification performance. This demonstrates the effectiveness of the proposed technique for the practical application in the extraction of information from multifrequency polarimetric images of urban areas.

APPENDIX A

MOMENTS OF THE LIKELIHOOD RATIO

To evaluate the expression of the moments of Λ , observe that Λ depends only on the two random matrices Σ_A and Σ_B . Assuming that the random polarimetric vectors describing the polarimetric echo from each pixel are independent, Σ_A and Σ_B are also independent and follow the complex Wishart distribution with $N_i, i = A, B$ degrees of freedom and covariance matrix \mathbf{R}

$$p_{\Sigma_i}(\Sigma_i) = \frac{|\Sigma_i|^{N_i-M}}{\tilde{\Gamma}_m(N_i)|\mathbf{R}|^{N_i}} \exp[-\text{Tr}(\mathbf{R}^{-1}\Sigma_i)], \quad \Sigma_i > 0. \quad (\text{A1})$$

Therefore, the h th moment becomes

$$\begin{aligned} \langle \Lambda^h \rangle &= C^{Mh} \int \int_{\Sigma_A, \Sigma_B > 0} \frac{|\Sigma_A|^{hN_A} |\Sigma_B|^{hN_B}}{|\Sigma|^{hN}} \\ &\quad \times p_{\Sigma_A}(\Sigma_A) p_{\Sigma_B}(\Sigma_B) d\Sigma_A d\Sigma_B \\ &= C^{Mh} |\mathbf{R}|^{hN} \frac{\tilde{\Gamma}_m[N_A(1+h)]}{\tilde{\Gamma}_m(N_A)} \frac{\tilde{\Gamma}_m[N_B(1+h)]}{\tilde{\Gamma}_m(N_B)} \\ &\quad \times \int \int_{\Sigma_A, \Sigma_B > 0} |\Sigma|^{-hN} \\ &\quad \cdot \frac{|\Sigma_A|^{N_A(1+h)-M}}{\tilde{\Gamma}_m[N_A(1+h)]|\mathbf{R}|^{N_A(1+h)}} \exp[-\text{Tr}(\mathbf{R}^{-1}\Sigma_A)] \\ &\quad \times \frac{|\Sigma_B|^{N_B(1+h)-M}}{\tilde{\Gamma}_m[N_B(1+h)]|\mathbf{R}|^{N_B(1+h)}} \\ &\quad \times \exp[-\text{Tr}(\mathbf{R}^{-1}\Sigma_B)] d\Sigma_A d\Sigma_B. \end{aligned} \quad (\text{A2})$$

The integration is equal to the expected value of $|\Sigma_A + \Sigma_B|^{-hN}$ over the distribution of two independent matrices Σ_A and Σ_B that follow the complex Wishart distribution with $N_i(1+h)$ degrees of freedom and covariance matrix \mathbf{R} . Therefore, $\Sigma_A + \Sigma_B$ follows the complex Wishart distribution with $N(1+h)$ degrees of freedom and covariance matrix \mathbf{R} . Thus, the moment can be rewritten as

$$\begin{aligned} \langle \Lambda^h \rangle &= C^{Mh} |\mathbf{R}|^{hN} \frac{\tilde{\Gamma}_m[N_A(1+h)]}{\tilde{\Gamma}_m(N_A)} \frac{\tilde{\Gamma}_m[N_B(1+h)]}{\tilde{\Gamma}_m(N_B)} \\ &\quad \times \int \int_{\Sigma_A, \Sigma_B > 0} |\Sigma|^{-hN} \frac{|\Sigma|^{N(1+h)-M}}{\tilde{\Gamma}_m[N(1+h)]|\mathbf{R}|^{N(1+h)}} \\ &\quad \times \exp[-\text{Tr}(\mathbf{R}^{-1}\Sigma)] d\Sigma \\ &= C^{Mh} \frac{\tilde{\Gamma}_m[N_A(1+h)]}{\tilde{\Gamma}_m(N_A)} \frac{\tilde{\Gamma}_m[N_B(1+h)]}{\tilde{\Gamma}_m(N_B)} \frac{\tilde{\Gamma}_m[N]}{\tilde{\Gamma}_m[N(1+h)]} \end{aligned} \quad (\text{A3})$$

which is the result reported in (16).

APPENDIX B

ASYMPTOTIC PDF FOR THE LIKELIHOOD RATIOS Λ_M AND Φ_M

The moment-generating function of $t = -\rho_M \ln \Lambda_M$ can be obtained as

$$\begin{aligned} M_t(s) &= E\{e^{-st}\} = E\{e^{s\rho_M \ln \Lambda_M}\} \\ &= E\{\Lambda_M^{s\rho_M}\} = E\{\Lambda_M^h\}|_{h=s\rho_M}. \end{aligned} \quad (\text{B1})$$

Using (16) and (A3), we get (B2) (shown at the bottom of the page) where $K = (\tilde{\Gamma}_m[N]\pi^{M(M-1)/2})/(\tilde{\Gamma}_m(N_A)\tilde{\Gamma}_m(N_B))$. To proceed further, we rewrite the argument of the three Gamma

$$M_t(s) = C^{M\rho_M s} K \frac{\prod_{i=1}^M \Gamma[N_A(1+\rho_M s) - i + 1] \Gamma[N_B(1+\rho_M s) - i + 1]}{\prod_{i=1}^M \Gamma[N(1+\rho_M s) - i + 1]} \quad (\text{B2})$$

functions in (B2) as $z + a$, where $z = \rho_M N_i(1+s)$ and a contains the remaining terms. Then, we use the asymptotic expression

$$\log \Gamma(z + a) = (z + a - 1/2) \log z - z + 1/2 \log 2\pi + \frac{1}{2z} \left(a^2 - a + \frac{1}{6} \right) + O(z^{-2}) \quad (\text{B3})$$

which yields for the logarithm in (B2)

$$\begin{aligned} \log M_t(s) &= -\frac{M^2}{2} \log(1+s) + \frac{M}{2\rho_M} \\ &\times \left[\frac{M^2-1}{6} \left(\frac{1}{N_A} + \frac{1}{N_B} - \frac{1}{N} \right) - M(1-\rho_M) \right] \\ &\times \left(\frac{1}{(1+s)} - 1 \right) + O\left(\frac{1}{\rho_M^2 N^2} \right). \end{aligned} \quad (\text{B4})$$

As apparent, by setting ρ_M as in (18), the second contribution to (B4) is nulled, and a simple asymptotic expression is obtained with error of the order of N^{-2}

$$\log M_t(s) = -\frac{M^2}{2} \log(1+s) + O\left(\frac{1}{\rho_M^2 N^2} \right). \quad (\text{B5})$$

When considering the model-based split-merge test, we need the pdf of $\tau = t_A + (\rho_{M_1}/\rho_{M_2})t_B$, where t_A and t_B are independent random variables that follow a Gamma distribution with order parameters $M_1^2/2$ and $M_2^2/2$, respectively. Therefore, the approximate expression of the pdf of τ is given by the inverse Laplace transform of

$$M_\tau(s) = \frac{1}{(1+s)^{M_1^2/2} \left(1 + \frac{\rho_{M_2}}{\rho_{M_1}} s \right)^{M_2^2/2}}. \quad (\text{B6})$$

By using the expansion of the rational function in (B6), we obtain

$$M_\tau(s) = \sum_{k=1}^{M_1^2/2} \frac{A_k}{(1+s)^k} + \sum_{j=1}^{M_2^2/2} \frac{B_j}{\left(1 + \frac{\rho_{M_2}}{\rho_{M_1}} s \right)^j} \quad (\text{B7})$$

where

$$\begin{aligned} A_k &= (-1)^{M_1^2/2-k} \binom{M_1^2/2 + M_2^2/2 - k - 1}{M_1^2/2 - k} \\ &\times \left(\frac{\rho_{M_2}}{\rho_{M_1}} \right)^{M_1^2/2-k} \left(1 - \frac{\rho_{M_2}}{\rho_{M_1}} \right)^{-M_1^2/2 - M_2^2/2 + k} \\ B_j &= (-1)^{M_2^2/2-j} \binom{M_1^2/2 + M_2^2/2 - j - 1}{M_2^2/2 - j} \\ &\times \left(\frac{\rho_{M_1}}{\rho_{M_2}} \right)^{M_2^2/2-j} \left(1 - \frac{\rho_{M_1}}{\rho_{M_2}} \right)^{-M_1^2/2 - M_2^2/2 + j} \end{aligned} \quad (\text{B8})$$

The inverse transform is straightforward

$$\begin{aligned} p_\tau(x) &= \sum_{k=1}^{M_1^2/2} \frac{A_k}{(k-1)!} x^{k-1} e^{-x} \\ &+ \sum_{j=1}^{M_2^2/2} \frac{B_j}{(j-1)!} \left(\frac{\rho_{M_1}}{\rho_{M_2}} \right)^j x^{j-1} e^{-\frac{\rho_{M_1}}{\rho_{M_2}} x} \end{aligned} \quad (\text{B9})$$

and the resulting P_{fa} is reported in (24).

ACKNOWLEDGMENT

The authors acknowledge the partial support of the Italian Space Agency (ASI) and many useful discussions with C. J. Oliver (InfoSAR).

REFERENCES

- [1] C. J. Oliver and S. Quegan, *Understanding SAR Images*, MA: Artech House, 1998.
- [2] J. J. Van Zyl, H. A. Zebker, and C. Elachi, "Imaging radar polarization signatures: Theory and observations," *Radio Sci.*, vol. 22, pp. 529–543, 1987.
- [3] F. T. Ulaby and C. Elachi, *Radar Polarimetry for Geoscience Applications*. Norwood, MA: Artech House, 1990.
- [4] H. A. Zebker and J. J. Van Zyl, "Imaging radar polarimetry: A review," *Proc. IEEE*, vol. 79, pp. 1583–1606, Nov. 1991.
- [5] L. M. Novak and M. C. Burl, "Optimal speckle reduction in polarimetric SAR imagery," *IEEE Trans. Aerosp. Electron. Systems.*, vol. 26, pp. 293–305, Mar. 1990.
- [6] J. Lee, M. R. Grunes, and S. A. Mango, "Speckle reduction in multipolarization, multifrequency SAR imagery," *IEEE Trans. Geosci. Remote Sensing*, vol. 29, pp. 535–544, July 1991.
- [7] L. M. Novak, M. C. Burl, and W. W. Irving, "Optimal polarimetric processing for enhanced target detection," *IEEE Trans. Aerosp. Electron. Syst.*, vol. 29, pp. 234–244, Jan. 1993.
- [8] S. R. Cloude and E. Pottier, "A review of target decomposition theorems in radar polarimetry," *IEEE Trans. Geosci. Remote Sensing*, vol. 34, pp. 498–518, Mar. 1996.
- [9] —, "An entropy based classification scheme for land applications of polarimetric SAR," *IEEE Trans. Geosci. Remote Sensing*, vol. 35, pp. 68–78, Jan. 1997.
- [10] J.-S. Lee and K. W. Hoppel, "Principal components transformation of multifrequency polarimetric SAR imagery," *IEEE Trans. Geosci. Remote Sensing*, vol. 30, pp. 686–696, July 1992.
- [11] T. Macri Pellizzeri, C. J. Oliver, and P. Lombardo, "Segmentation-based joint classification of SAR and optical images," *Proc. Inst. Elect. Eng.—Radar Sonar and Navigat.*, vol. 149, no. 6, pp. 281–296, Dec. 2003.
- [12] P. Lombardo and C. J. Oliver, "Optimal classification of polarimetric SAR images using segmentation," in *Proc. IEEE Radar Conf. 2002*, Long Beach, CA, Apr. 2002.
- [13] —, "Optimal polarimetric segmentation for the classification of agricultural areas," in *Proc. EUSAR 2002*, Koeln, Germany, June 2002.
- [14] A. Freeman, J. J. van Zyl, J. D. Klein, H. A. Zebker, and Y. Shen, "Calibration of Stokes and scattering matrix format polarimetric SAR data," *IEEE Trans. Geosci. Remote Sensing*, vol. 30, pp. 531–539, Mar. 1992.
- [15] P. Lombardo and C. J. Oliver, "Optimum detection and segmentation of oil-slicks using polarimetric SAR data," in *Proc. Inst. Electron. Eng.—Radar, Sonar Navigat.*, vol. 147, Dec. 2000.
- [16] *Handbook of Mathematical Functions*, Dover, New York, 1964.
- [17] C. J. Oliver, I. McConnell, and D. G. Corr, "Multi-temporal change detection for SAR imagery," in *Proc. SPIE Europto Conf. SAR Image Analysis, Modeling and Techniques IV*, vol. 3869, Florence, Italy, 1999.
- [18] P. Lombardo and T. Macri Pellizzeri, "Maximum likelihood signal processing techniques to detect a step pattern of change in multitemporal SAR images," *IEEE Trans. Geosci. Remote Sensing*, vol. 40, pp. 853–870, Apr. 2002.
- [19] T. Macri Pellizzeri, P. Gamba, P. Lombardo, and F. Dell'Acqua, "Multi-temporal/multiband SAR classification of urban areas using spatial analysis: Statistical vs. neural kernel-based approach," *IEEE Trans. Geosci. Remote Sensing*, submitted for publication.
- [20] J.-S. Lee, M. R. Grunes, and S. A. Mango, "Speckle reduction in multipolarization, multifrequency SAR imagery," *IEEE Trans. Geosci. Remote Sensing*, vol. 29, pp. 535–544, July 2000.
- [21] L. Ferro-Famil, E. Pottier, and J.-S. Lee, "Unsupervised classification of multi-frequency, fully polarimetric SAR images based on the H/A/alpha-Wishart classifier," *IEEE Trans. Geosci. Remote Sensing*, vol. 39, pp. 2332–2342, Nov. 2001.



Pierfrancesco Lombardo (S'93–M'95) received the laurea degree in electronic engineering and the Ph.D. degree from the University of Rome "La Sapienza," Rome, Italy, in 1991 and 1995, respectively.

In 1994, he was a Research Associate at the University of Birmingham, Birmingham, U.K., while also with the SAR team of the Defense Research Agency, Malvern, U.K. He was involved in research on space-time adaptive processing for AEW at Syracuse University, Syracuse, NY, where he was a Research Associate in 1996. In June

1996, he joined the University of Rome "La Sapienza," where he has been an Associate Professor since 1998. He is involved in research projects funded by the Italian Space Agency on multiparametric SAR image processing, and in projects on advanced radar detection, data fusion, and radiolocalization. He is also Co-Investigator of the radar sounding instruments for the space exploration missions Rosetta (ESA/ASI) and Mars Express (ASI/NASA). His research has been reported in over 80 publications in international technical journals and conferences.

Dr. Lombardo served in the paper selection committee of the IEEE Radar Conference 2001 (Atlanta, GA) and as Technical Chairman of the IEEE/ISPRS Joint Workshop on Remote Sensing and Data Fusion over Urban Areas (Rome 2001). He is Associate Editor for Radar Systems for the IEEE TRANSACTIONS ON AEROSPACE AND ELECTRONIC SYSTEMS. He received in 2001 the Barry Carlton Award for the best paper published in the IEEE TRANSACTIONS ON AEROSPACE AND ELECTRONIC SYSTEMS.



Massimo Sciotti was born in Rome, Italy, on November 3, 1973. He received the communication engineering degree from the University of Rome "La Sapienza," Rome, Italy, in 2000. He is currently pursuing the Ph.D. degree in remote sensing at the University of Rome "La Sapienza."

He served as an Engineer Officer in the Telecommunication Systems Maintenance Centre of the Italian Army, in 2001. His main research interests are in multichannel SAR image processing, non-Gaussian clutter and target modeling, CFAR

techniques, and advanced polarimetric radar detection techniques. He is currently involved in research activities on radar sounding instruments for archeological investigations (ground-penetrating radar) and for space exploration missions (sounding of the Mars regolith).



Tiziana Macrí Pellizzeri was born in Rome, Italy, in December 1975. She graduated with distinction in communication engineering from the University of Rome "La Sapienza," in July 2000. She is currently pursuing the Ph.D. degree in remote sensing at University of Rome "La Sapienza."

Her research activity includes multiparametric image processing, and in particular the fusion of SAR and optical images, and multifrequency polarimetric image processing. In 2000 and 2001, she has been involved in a national research project

on the fusion of SAR and optical images funded by the Italian Ministry of University and Research.

Ms. Macrí Pellizzeri is a member of the IEEE Geoscience and Remote Sensing Society Data Fusion Committee. She was the winner of the Student Paper Prize Competition at the 2001 IEEE Radar Conference (Atlanta, GA) in May 2001.

Marco Meloni was born in Rome, Italy, in 1975. He received the laurea degree in communication engineering from the University of Rome "La Sapienza," Rome, Italy, in July 2002.

During his graduation thesis, he developed and implemented different segmentation techniques for multitemporal SAR, polarimetric SAR, and multi-sensor images. He is currently attending his civil service, and he is collaborating with the "La Sapienza" INFOCOM Department on the development and the implementation of new segmentation techniques.